

Field-linear anomalous Hall effect and Berry curvature induced by spin chirality in the kagome antiferromagnet Mn_3Sn

Received: 25 June 2022

Accepted: 1 March 2023

Published online: 24 March 2023

 Check for updatesXiaokang Li¹✉, Jahyun Koo², Zengwei Zhu¹✉, Kamran Behnia³ & Binghai Yan²✉

During the past two decades, it has been established that a non-trivial electron wave-function topology generates an anomalous Hall effect (AHE), which shows itself as a Hall conductivity non-linear in magnetic field. Here, we report on an unprecedented case of field-linear AHE. In Mn_3Sn , a kagome magnet, the out-of-plane Hall response, which shows an abrupt jump, was discovered to be a case of AHE. We find now that the in-plane Hall response, which is perfectly linear in magnetic field, is set by the Berry curvature of the wavefunction. The amplitude of the Hall response and its concomitant Nernst signal exceed by far what is expected in the semiclassical picture. We argue that magnetic field induces out-of-plane spin canting and thereafter gives rise to nontrivial spin chirality on the kagome lattice. In band structure, we find that the spin chirality modifies the topology by gapping out Weyl nodal lines unknown before, accounting for the AHE observed. Our work reveals intriguing unification of real-space Berry phase from spin chirality and momentum-space Berry curvature in a kagome material.

Understanding the origin of anomalous Hall effect (AHE), observed as early as 1881 in ferromagnetic solids¹ has been enriched in the present century by considering the role played by the topology of electron wave-function^{2,3}. In a uniform magnet, the Berry curvature leads to anomalous velocity⁴ as a fictitious magnetic field in the momentum-space, which exhibits monopole-like texture⁵ around the Weyl point^{6,7}, and is extensively regarded the intrinsic source of AHE. In unconventional magnetic structures like skyrmions⁸, an electron hopping on non-coplanar spin lattice with spin chirality^{9–12} picks up a real-space Berry phase and also lead to a Hall response, which is commonly referred to as the topological Hall effect (THE)^{13,14}. Both AHE and THE are characterized by a non-linear Hall resistivity. To the best of our knowledge, there is no report on anomalous Hall response without significant departure from field-linearity, believed to be a

necessary ingredient for separating ordinary and unusual components of the Hall response. Here, we present a counter-example to this common belief.

Recent theoretical predictions of a large intrinsic AHE in non-collinear antiferromagnets with a nearly compensated magnetization^{15–17} was followed by the experimental discovery of sizeable room-temperature AHE in Mn_3X ($\text{X} = \text{Sn}$ and Ge)^{18–20} and its counterparts, such as the anomalous Nernst^{21,22}, thermal Hall^{22–24} and magneto-optical Kerr effect^{25,26}, as well as topological and planar Hall effects^{27–30}, which appear in presence of the topologically non-trivial domain walls³¹ of this magnet. Since the scalar spin-chirality vanishes in the co-planar spin texture, the AHE can solely be understood by the Berry curvature^{15–17} with the co-existence of Weyl points^{6,32} in the band structure. Potential applications are identified in a variety of fields such as antiferromagnetic spintronics^{33–36} and transverse thermopiles^{21,37}.

¹Wuhan National High Magnetic Field Center and School of Physics, Huazhong University of Science and Technology, Wuhan 430074, China.

²Department of Condensed Matter Physics, Weizmann Institute of Science, 7610001 Rehovot, Israel. ³Laboratoire de Physique et d'Étude des Matériaux (ESPCI—CNRS—Sorbonne Université), PSL Research University, 75005 Paris, France. ✉e-mail: lixiaokang@hust.edu.cn; zengwei.zhu@hust.edu.cn; binghai.yan@weizmann.ac.il

More recently, intriguing AHE was also extensively studied in emerging kagome materials such as AV_3Sb_5 ($A = K, Rb, Cs$)^{38,39} and RMn_6Sn_6 (R is a rare earth element)^{40–42}.

Mn_3X ($X = Sn$ and Ge) are antiferromagnetic at room temperature, with spins residing inside kagome planes of the crystal^{18,43}. When the magnetic field is perpendicular to these planes, neither the magnetization nor the Hall resistivity show a jump. Previous studies have assumed that non-trivial topology of the electronic wave-function does not reveal itself in this configuration due to symmetry constrain of the planar spin texture^{6,16–18}.

In this work, by measuring the transverse electric and thermoelectric coefficients up to 14 T, we show that the in-plane field-linear Hall number of Mn_3Sn , is five times larger than what is expected from the carrier density and the Nernst signal is two orders of magnitude larger than what expected given the mobility and the Fermi energy of the system. We reveal an additional hidden component dominating the ordinary signals in both cases. Our theoretical calculations reveal that out-of-plane spin canting⁴⁴ induced by the magnetic field leads to nonzero spin chirality and simultaneously generates Berry curvature by gapping Weyl nodal lines unrecognized before. Our results present a unified mechanism between the real-space and momentum-space Berry phases as the origin of this unusual field-linear Hall effect.

Results

Field induced linear anomalous Hall effect

Figure 1 shows how drastically the Hall resistivity in Mn_3Sn depends on the configuration. When the magnetic field, parallel to the kagome planes, is swept from negative to positive values (Fig. 1a), the ρ_{zy} Hall resistivity displays a jump (Fig. 1c). However, when the field is perpendicular to the planes (Fig. 1b), the ρ_{xy} Hall response is perfectly linear as a function of magnetic field. Figure 1c shows this drastic difference between out-of-plane (ρ_{zy}) and in-plane (ρ_{xy}) Hall resistivities at 200 K.

Scrutinizing ρ_{zy} , one can see that it consists of two parts. The first is the anomalous Hall resistivity ρ_{zy}^A , which has a spontaneous amplitude of $4.2 \mu\Omega\text{cm}$ at 0 T. The second is the ordinary Hall resistivity, ρ_H^O , which attains the amplitude of $0.77 \mu\Omega\text{cm}$, when the field is swept from 0 T to 14 T. It corresponds to a carrier density of $n = 1.14 \cdot 10^{22} \text{cm}^{-3}$, consistent with previous reports^{18,22} and the theoretically calculated carrier density²⁷. At the first sight, ρ_{xy} , which is linear in magnetic field, looks like an ordinary Hall response. However, its amplitude, as large as $3.9 \mu\Omega\text{cm}$ at 14 T, is five times larger than ρ_H^O and is incompatible with the large carrier density of the system. Note that invoking the presence of carriers of both signs would pull down the Hall number and does not provide a solution for the puzzle of an anomalously large Hall number.

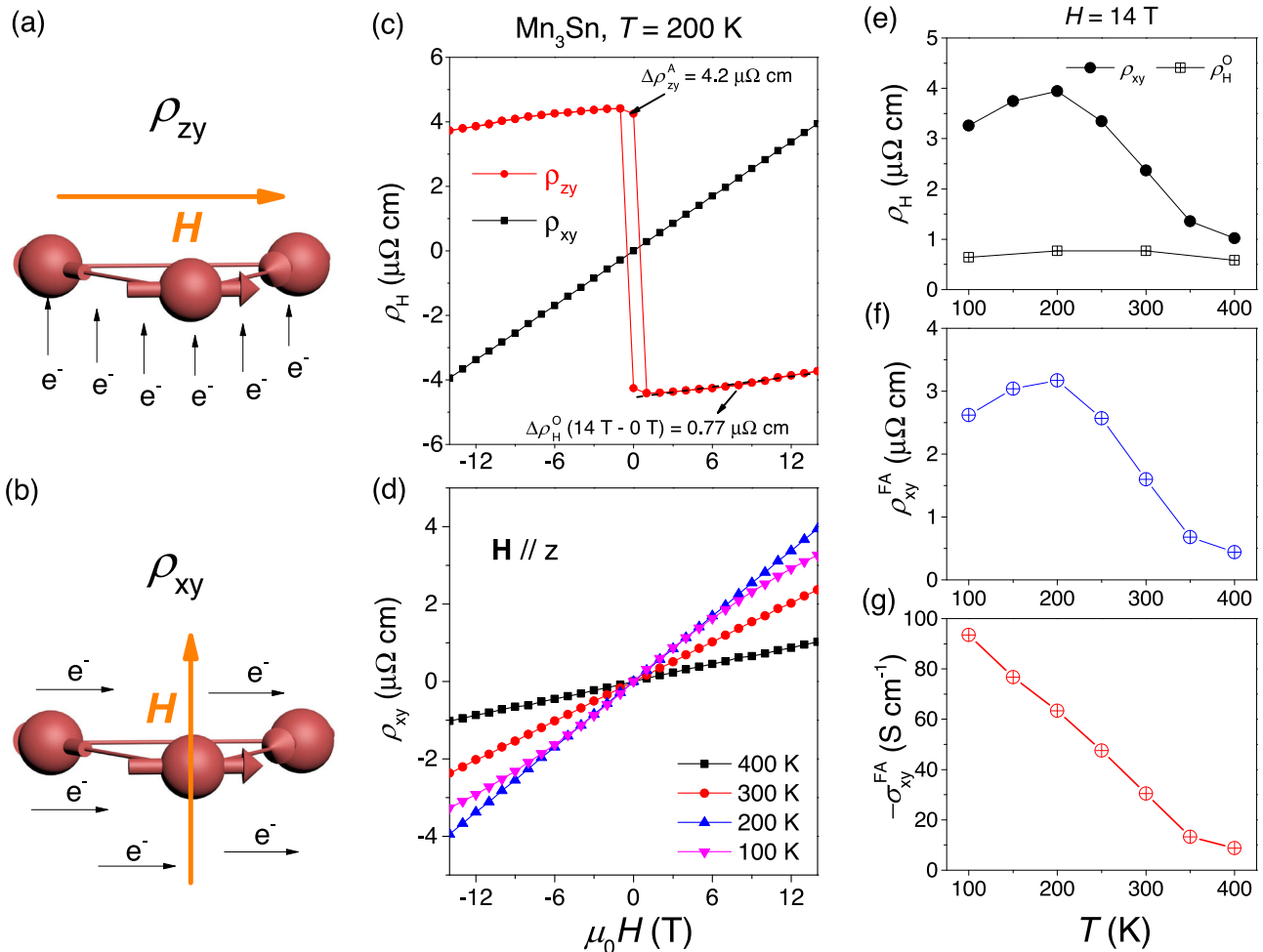


Fig. 1 | Field induced anomalous Hall effect. **a, b** Different Hall configurations. ρ_{zy} , the out-of-plane Hall configuration with the field along x axis. ρ_{xy} , the in-plane Hall configuration with the field along z axis. **c** Comparison of out-of-plane (ρ_{zy}) and in-plane (ρ_{xy}) Hall responses. ρ_{zy} consists of two parts, the anomalous Hall resistivity ρ_{zy}^A with a spontaneous value of $4.2 \mu\Omega\text{cm}$ at 0 T, and the ordinary Hall resistivity ρ_H^O with a value of $0.77 \mu\Omega\text{cm}$ when the field is swept from 14 T to 0 T. ρ_{xy} , looking like

ordinary Hall effect attains $3.9 \mu\Omega\text{cm}$ at 14 T, exceeding ρ_H^O by far. **d** Field dependence of ρ_{xy} with temperature varying from 100 to 400 K. **e** Temperature dependence of ρ_{xy} and ρ_H^O at 14 T. **f** Temperature dependence of field-induced linear anomalous Hall resistivity ρ_{xy}^{FA} . **g** Temperature dependence of field-induced linear anomalous Hall conductivity σ_{xy}^{FA} (see the Supplementary Information for calculation details). It is monotonously increasing with cooling.

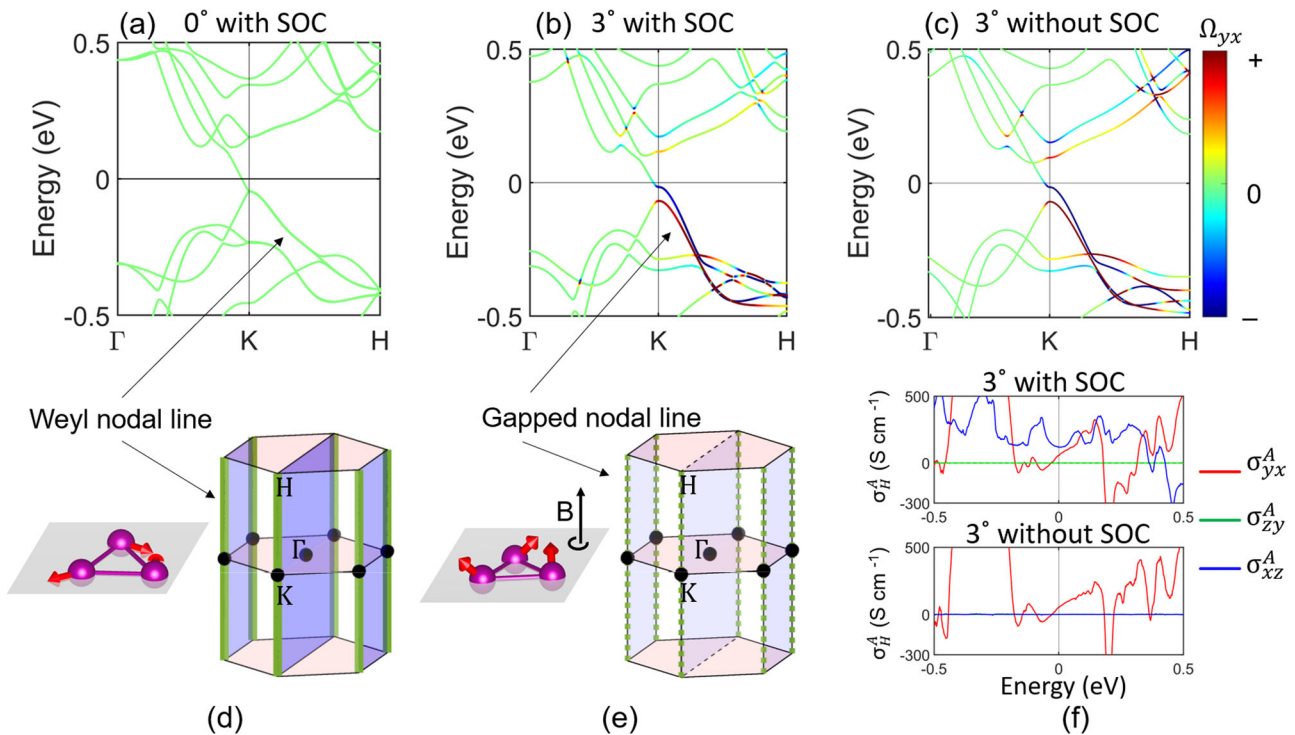


Fig. 2 | Spin canting gaps out Weyl nodal lines and pushes Berry curvature to the Fermi surface. **a, b** Band structures without and with spin canting (3°), respectively. **c** Band structure with 3° canting but excluding SOC. The color bar represents the amplitude of Berry curvature Ω_{yx} . Without spin canting, there is a doubly-degenerate (weakly gapped by SOC) Weyl nodal line dispersing along the $K-H$ axis (including the K point) in the Brillouin zone, as indicated by the solid

green line in **d**. Spin canting significantly gaps out the nodal line, as indicated by the dashed green line in **e**, and induces giant Berry curvature Ω_{yx} on split bands in **b** and **c**. The mirror planes [M_x , blue planes in **d**] without spin canting forces $\Omega_{yx} = 0$ inside the plane. The Fermi energy is shifted to zero. **f** The Fermi energy-dependent anomalous Hall conductivities for 3° canting. σ_{yx}^A is dominantly contributed by the spin chirality while σ_{zy}^A relies on SOC.

We will see below that the large amplitude of ρ_{xy} includes a hidden topological component.

Figure 1d shows the field dependence of ρ_{xy} at different temperatures varying from 100 to 400 K. Note the drastic diminished amplitude of the 400 K curve. Figure 1e shows the temperature dependence of $\rho_H^0(14\text{ T})$ and $\rho_{xy}(14\text{ T})$. As expected, $\rho_H^0(14\text{ T})$ is flat over a wide temperature range, consistent with its identified origin. Indeed, the Fermi surface topology and the carrier density do not vary with cooling. On the other hand, $\rho_{xy}(14\text{ T})$ shows a strong temperature dependence and decreases rapidly with warming. As the Néel temperature ($T_N = 420\text{ K}$) is approached, it becomes close to ρ_H^0 . This implies that the temperature-independent ordinary Hall effect is almost isotropic and $\rho_{xy}(14\text{ T})$ acquires another component below T_N . This additional component, which we call field-induced linear anomalous Hall resistivity (FILAHE) ρ_{xy}^{FA} , be quantified by extracting ρ_H^0 from $\rho_{xy}(14\text{ T})$. Figure 1f shows this FILAHE, ρ_{xy}^{FA} . Its conductivity counterpart, σ_{xy}^{FA} , is shown in Fig. 1g. It is monotonously increasing with cooling.

Before presenting a theoretical explanation, let us briefly notice that the anomalous nature of the Hall response produced by an out-of-plane magnetic field was overlooked by previous studies. In 2016, Nayak et al.¹⁹ measured the Hall responses of Mn_3Ge up to 5 T for three different configurations and found that when the field is along the z direction, the slope is significantly larger. More recently, a review of the transport properties of Mn_3X ($X = \text{Sn, Ge}$) contrasted the absence of hysteresis in ρ_{xy} with its presence in ρ_{yz} and ρ_{zx} .⁴⁵

Spin canting gaps out Weyl nodal lines and pushes Berry curvature to the Fermi surface

Assuming that magnetic field modifies the spin structure can provide an explanation for this finite σ_{xy}^{FA} . Such an assumption is supported by a recent torque magnetometry study in Mn_3Sn .⁴⁴ Magnetic field favors

alignment of spins along its orientation. When it rotates in the basal plane, this Zeeman effect would enter a competition with three other energy scales of the system (Heisenberg, Dzyaloshinskii-Moriya and Single-ion-anisotropy)³¹ in order to generate a non-trivial twist of spins⁴⁶, giving rise to additional odd terms in the magnetic free energy⁴⁴. Modification of the spin orientation by an *out-of-plane* magnetic field provides a hidden source of Hall response.

In symmetry analysis, the AHE XY component (σ_{xy}^A) without spin canting is strictly prohibited because the combined symmetry (TM_z) by time-reversal (T) and mirror reflection ($M_z: z \rightarrow -z$) constrains the Berry curvature Ω_{xy} to be opposite between (k_x, k_y, k_z) and $(-k_x, -k_y, k_z)$. Further, σ_{xy}^A vanishes also because a vertical glide mirror $\widetilde{M}_x \equiv \{M_x | \frac{z}{2}\}$ forces opposite Ω_{xy} between (k_x, k_y, k_z) and $(k_x, -k_y, k_z)$. In the band structure, there is a seemingly crossing point at the K point slightly below the Fermi energy (Fig. 2a), which was recognized as a Weyl point in some earlier studies. However, it is impossible to host a Weyl point at K , because the mirror plane would reverse the Weyl point chirality. At K , a tiny gap is actually opened by spin-orbit coupling (SOC). Without SOC, we find a doubly-degenerate nodal line, referred to as the Weyl nodal line, along the $K-H$ axis in the Brillouin zone (see Supplementary Fig. 2). Then, SOC induces tiny hybridization gaps along the nodal line. Along $\Gamma-K-H$, however, Ω_{xy} is always zero (Fig. 2a) because of the M_x mirror plane.

After spin canting or spin chirality appears and breaks both \widetilde{M}_x and TM_z symmetries, the XY AHE emerges. In the band structure, the symmetry reduction significantly enlarges the energy gap along the Weyl nodal line. More importantly, spin canting generates a large Berry curvature Ω_{xy} along the nodal line. Because the gap is large, Ω_{xy} is smeared out and reaches the Fermi surface, as shown in Fig. 2b. Therefore, the net Berry curvature at the Fermi surface, and its associate anomalous Hall conductivity σ_{xy}^A , emerge. On the other hand,

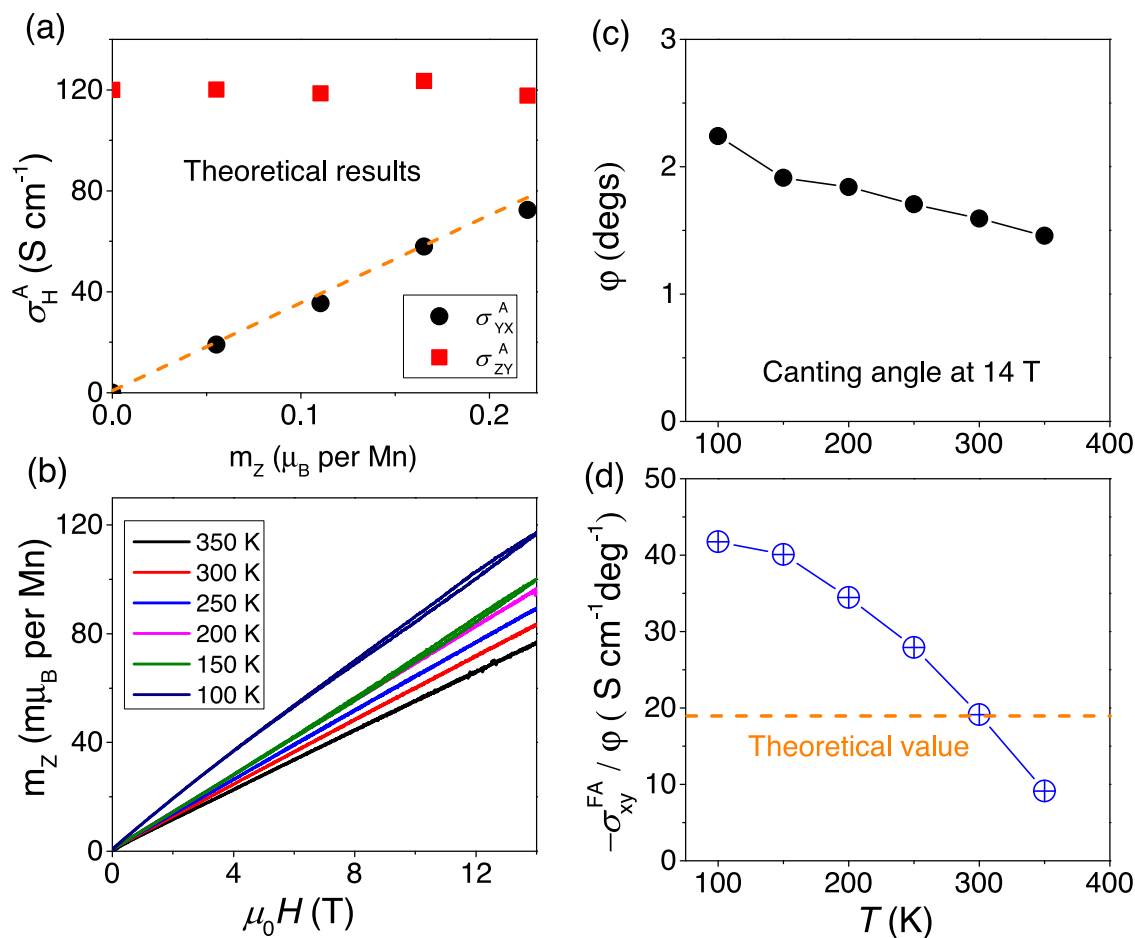


Fig. 3 | Comparison between theory and experiment. **a** Comparison of the theoretical calculated anomalous Hall conductivity in different Hall configurations (YX and ZY). The σ_{ZY}^A shows a flat behavior, but the σ_{YX}^A shows a fast increasing with the m_z . **b** The field dependent canting moment (m_z) with temperature varying from 350

to 100 K. **c** Temperature dependence of the canting angle ϕ , calculated from data in **b** and by formula $\arcsin(m_z/3\mu_B)$. **d** The ratio of σ_{xy}^A to the canting angle at different temperatures.

the scalar spin chirality (χ) is linearly proportional to canting spin angle, e.g., $\chi = \mathbf{S}_1 \cdot (\mathbf{S}_2 \times \mathbf{S}_3)$ where $\mathbf{S}_{1,2,3}$ are spins in a triangle, in the small tilting limit. Spin chirality can generate a real-space Berry phase when an electron hops between spin sites. To validate the role of spin chirality in AHE, we calculated the band structure and Berry curvature by excluding SOC. As shown in Fig. 2c, one can find that the Berry curvature and band structure remain almost the same as the SOC case (Fig. 2b), where SOC merely lifts some degeneracy in the band structure. In the absence of SOC, σ_{yx}^A is nearly unchanged while σ_{yz}^A becomes zero (see Fig. 2f). Therefore, the spin chirality-induced Hall response (σ_{yx}^A) coincides (rather than adds up to) with the AHE derived from the Berry curvature. In addition, Weyl points may exist near the nodal line gap due to accidental band crossing, for example, among bands near -0.3 eV which marginally affect the Fermi surface. The nodal line gap near the K point is the main, direct Berry curvature origin to the AHE observed, which is further indicated by the Fermi energy-dependence of the anomalous Hall conductivity in Fig. 2f (also Supplementary Fig. 3). In addition, we showed the spin-canting induced anomalous Nernst coefficient in Supplementary Fig. 4.

Comparison between theory and experiment

The canting angle of spins cannot be directly probed by our experiment. However, a reasonable assumption is to compare the theoretical canting with the experimentally resolved field-linear magnetization when the field is oriented along the z-axis^{31,44}. As seen in Fig. 3b, this magnetization changes from 80 to 120 $m\mu_B$ per Mn atom at

14 T between 100 to 400 K. Assuming that this is entirely caused by the field-induced canting of spins (i.e., neglecting any zero-field canting of spins), it would correspond to a canting angle (ϕ) of the order of ~ 2 degrees. Figure 3c shows the canting angle estimated in this way at different temperatures. Figure 3d shows the evolution of the ratio σ_{xy}^A / ϕ at different temperatures. One can see that there is an agreement in order of magnitude. However, the experimentally resolved temperature dependence of σ_{xy}^A / ϕ is not captured by our model. This points to a missing ingredient, yet to be identified. We note that the canting angle of spins remains unmeasured. Our estimation was based on the amplitude of the out-of plane magnetization, which in presence of finite transverse magnetic susceptibility, may not be strictly accurate. Future studies of spin texture in presence of magnetic field may settle this discrepancy.

It is worth noting that the cluster multipole theory may also apply to our findings. Suzuki et al.⁴⁷ proposed that the in-plane octupole moment T_x^y (T_y^x) is lower than the three-dimensional octupole moment T_{xyz} (T_z^y) in each cluster, and the neighboring clusters have ferromagnetic (net) and antiferromagnetic (vanished) alignments respectively. Out-of-plane spin canting may induce a finite T_{xyz} (T_z^y) between neighboring clusters and generates FILAHE.

Field induced linear anomalous Nernst effect

Our interpretation is further supported by our measurements of the Nernst effect. Figure 4a, b shows the field dependence of the Nernst signal S_{xy} and the transverse thermoelectric conductivity α_{xy} up to 14 T

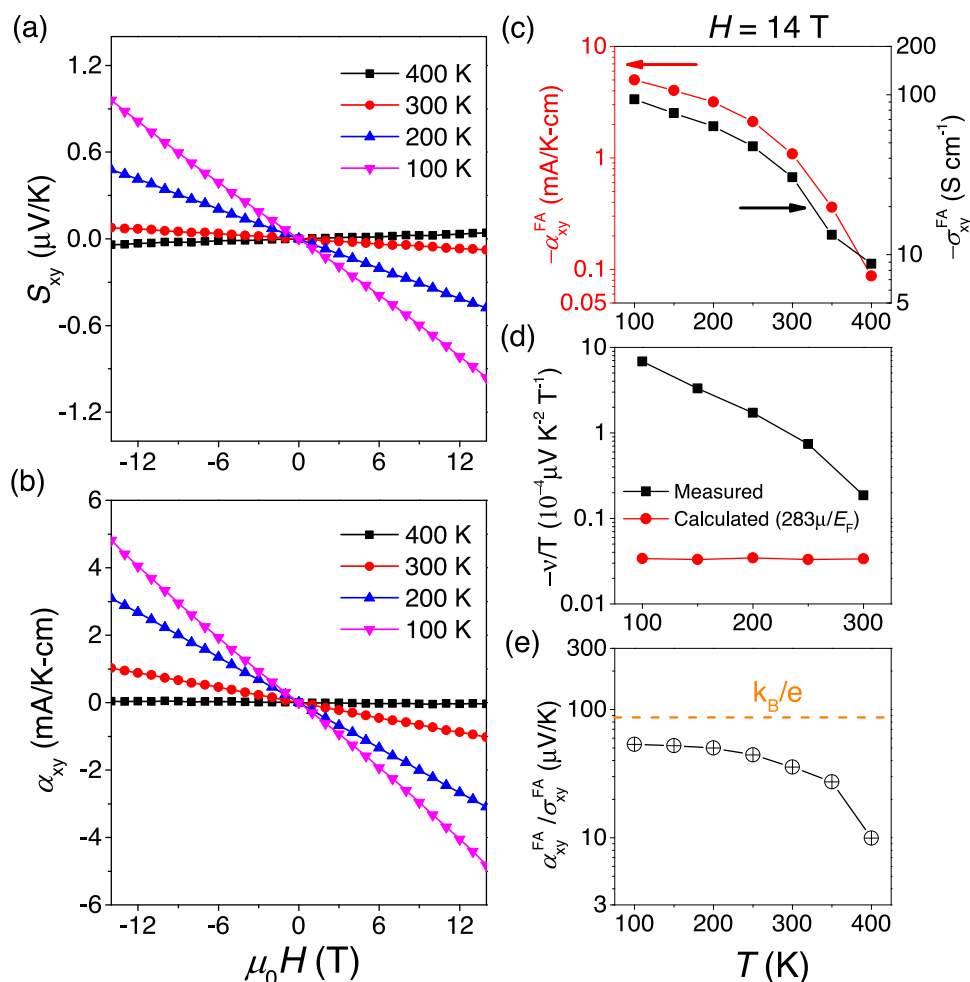


Fig. 4 | Field induced anomalous Nernst effect. **a, b** Field dependence of S_{xy} and α_{xy} up to 14 T, with temperature varying from 100 to 400 K. **c** Comparison of temperature dependence of σ_{xy}^{FA} and α_{xy}^{FA} at 14 T. **d** Temperature dependence of the Nernst coefficient ($\nu = S_{xy}/H$) divided by temperature. Measured Nernst signal (the black squares) with the largest value of $6.85 \cdot 10^{-4} \mu\text{VK}^{-2} \text{T}^{-1}$, becomes two orders of

magnitude larger than the estimated ordinary Nernst signal (the red circles) $3.45 \cdot 10^{-6} \mu\text{VK}^{-2} \text{T}^{-1}$ estimated by $283\mu/E_F$, here μ and E_F are carrier mobility and Fermi energy. **e** Temperature dependence of the ratio of off-diagonal field induced anomalous Hall and Nernst conductivity ($\alpha_{xy}^{FA}/\sigma_{xy}^{FA}$).

as the temperature changes from 100 to 400 K. As seen in Fig. 4c, the Nernst response, like the Hall response but more drastically, decreases with warming and approaching the Néel temperature. At 400 K, the former disappears, but the latter remains finite. As seen in Fig. 4d, the measured Nernst signal becomes two orders of magnitude larger than what is theoretically expected for the amplitude of the ordinary Nernst signal and experimentally observed in a variety of solids⁴⁸.

This, the amplitude of the Nernst response is incompatible with an ordinary origin. On the other hand, it does correspond to what is expected in a topological picture of the amplitude of anomalous transverse thermoelectric conductivity^{49,50}. Indeed, in topological magnets, the amplitude of the anomalous Nernst signal anti-correlates with mobility⁴⁹ and the amplitudes of the anomalous Hall and Nernst conductivities correlate with each other⁵⁰. In the case of the field-induced signals observed here, we found that $\alpha_{xy}^{FA}/\sigma_{xy}^{FA}$, varies from 10 $\mu\text{V/K}$ at 400 K to 53 $\mu\text{V/K}$ at 100 K, approaching $k_B/e = 86 \mu\text{V/K}$. Such a behavior has been observed in a variety of other magnets displaying anomalous transverse response⁵⁰.

In summary, we found a new variety of anomalous Hall effect and its Nernst counterpart induced by magnetic field. We showed that spin chirality induces Berry curvature on the Fermi surface by gapping the Weyl nodal line, resulting in the field-induced linear anomalous transverse response.

Methods

Samples

The centimeter-size Mn_3Sn crystal was grown by the vertical Bridgman technique²⁷. Firstly, the raw materials (99.999% Mn, 99.999% Sn) with the molar ratio of 3.3 : 1 were heated up to 1100 °C for the precursor crystal growth. Secondly, the precursor crystal power was put in an alumina crucible and sealed in a quartz tube and hung in a vertical Bridgman furnace for the single crystal growth. The growth procedure was repeated three times with different rates such as 2, 2 and 1 mm/h to purify the crystal. Using the energy dispersive X-ray spectroscopy (EDX), the stoichiometry of single crystal was found to be $\text{Mn}_{3.22}\text{Sn}$, close to but slightly below the ratio of the raw materials³⁷. Finally, the large size single crystal was cut to desired dimension sample, such as 2.5 mm \times 1.6 mm \times 0.1 mm used in this work, by a wire saw.

Measurements

All transport experiments were performed in a commercial measurement system (Quantum Design PPMS). Electric transport responses were measured by a standard four-probe method using a current source (Keithley6221) and a DC-nanovoltmeter (Keithley2182A). Thermoelectric transport responses were measured at a high vacuum environment, using a 4.7 k Ω chip resistor for the heater, a copper plate for the heat-sink, and a difference type E thermocouples for detecting

the temperature difference. Magnetization was measured by the vibrating sample magnetometer (VSM) mounted on PPMS. All measurements were performed on the same sample.

Calculations

We performed the density-functional theory (DFT) calculation follows in the framework of the generalized gradient approximation with the Vienna ab initio package. We employed the PBE-D2 method to describe vdW interaction. Spin-orbit coupling (SOC) was included in all calculations. The magnetic ground state of the Mn_3Sn , which has an antichiral triangular inplane spin structure with $3\mu_B$ magnetic moment for each Mn atom as same as in the experiment (Fig. 2b). Start from the inplane spin structure as canting angle 0° , we tilted the spin-direction to out of plane direction uniformly to imitate applying the magnetic field in the experiment (Fig. 2d). After the magnetic state relaxation we can find local minimum spin state with finite m_z magnetic moment.

We have projected the DFT Bloch wave function into Wannier functions to construct an effective Hamiltonian (\hat{H}) to evaluated the anomalous Hall conductivity:

$$\sigma_{ij}^k(\mu) = -\frac{e^2}{\hbar} \int_{\text{BZ}} \frac{d\mathbf{k}}{(2\pi)^3} \sum_{\epsilon_n < \mu} \Omega_{ij}^z(\mathbf{k}) \quad (1)$$

$$\Omega_{ij}^k(k) = i \sum_{m \neq n} \frac{\langle n | \hat{v}_i | m \rangle \langle n | \hat{v}_j | m \rangle - (j \leftrightarrow i)}{(\epsilon_n(\mathbf{k}) - \epsilon_m(\mathbf{k}))^2}. \quad (2)$$

$$\frac{\alpha_{xy}^A}{T} \Big|_{T \rightarrow 0} = -\frac{\pi^2 k_B^2}{3|e|} \frac{d\sigma_{xy}^A}{d\mu}, \quad (3)$$

Here μ is the chemical potential and ϵ_n is the eigenvalue of the $|n\rangle$ eigenstate, and $\hat{v}_i = \frac{d\hat{H}}{d\mathbf{k}_i}$ ($i = x, y, z$) is the velocity operator. A k -point of grid of $100 \times 100 \times 100$ is used for the numerical integration. Near the zero temperature, the anomalous Nernst coefficient follows the Mott relation.

Data availability

The data that support the findings of this study are available from the corresponding author upon reasonable request.

References

- Hall, E. H. On the "Rotational Coefficient" in Nickel and Cobalt. *Lond. Edinb. Dublin Philos. Mag. J. Sci.* **12**, 157–172 (1881).
- Nagaosa, N., Sinova, J., Onoda, S., MacDonald, A. H. & Ong, N. P. Anomalous Hall effect. *Rev. Mod. Phys.* **82**, 1539–1592 (2010).
- Xiao, D., Chang, M.-C. & Niu, Q. Berry phase effects on electronic properties. *Rev. Mod. Phys.* **82**, 1959–2007 (2010).
- Karplus, R. & Luttinger, J. M. Hall Effect in Ferromagnetics. *Phys. Rev.* **95**, 1154–1160 (1954).
- Volovik, G. E. *The Universe in a Helium Droplet*, Vol. 117 (OUP Oxford, 2003).
- Yang, H. et al. Topological Weyl semimetals in the chiral antiferromagnetic materials Mn_3Ge and Mn_3Sn . *N. J. Phys.* **19**, 015008 (2017).
- Armitage, N. P., Mele, E. J. & Vishwanath, A. Weyl and Dirac semimetals in three-dimensional solids. *Rev. Mod. Phys.* **90**, 015001 (2018).
- Nagaosa, N. & Tokura, Y. Topological properties and dynamics of magnetic skyrmions. *Nat. Nanotechnol.* **8**, 899–911 (2013).
- Wen, X. G., Wilczek, F. & Zee, A. Chiral spin states and superconductivity. *Phys. Rev. B* **39**, 11413–11423 (1989).
- Ye, J. et al. Berry Phase Theory of the Anomalous Hall Effect: Application to Colossal Magnetoresistance Manganites. *Phys. Rev. Lett.* **83**, 3737–3740 (1999).
- Ohgushi, K., Murakami, S. & Nagaosa, N. Spin anisotropy and quantum Hall effect in the kagomé lattice: Chiral spin state based on a ferromagnet. *Phys. Rev. B* **62**, R6065–R6068 (2000).
- Tatara, G. & Kawamura, H. Chirality-driven anomalous Hall effect in weak coupling regime. *J. Phys. Soc. Japan* **71**, 2613–2616 (2002).
- Taguchi, Y., Oohara, Y., Yoshizawa, H., Nagaosa, N. & Tokura, Y. Spin chirality, Berry phase, and anomalous Hall effect in a frustrated ferromagnet. *Science* **291**, 2573–2576 (2001).
- Neubauer, A. et al. Topological Hall effect in the A phase of MnSi . *Phys. Rev. Lett.* **102**, 186602 (2009).
- Chen, H., Niu, Q. & MacDonald, A. H. Anomalous Hall effect arising from noncollinear antiferromagnetism. *Phys. Rev. Lett.* **112**, 017205 (2014).
- Kübler, J. & Felser, C. Non-collinear antiferromagnets and the anomalous Hall effect. *EPL* **108**, 67001 (2014).
- Zhang, Y. et al. Strong anisotropic anomalous Hall effect and spin Hall effect in the chiral antiferromagnetic compounds Mn_3X ($X = \text{Ge}, \text{Sn}, \text{Ga}, \text{Ir}, \text{Rh}, \text{and Pt}$). *Phys. Rev. B* **95**, 075128 (2017).
- Nakatsuji, S., Kiyohara, N. & Higo, T. Large anomalous Hall effect in a non-collinear antiferromagnet at room temperature. *Nature* **527**, 212–215 (2015).
- Nayak, A. K. et al. Large anomalous Hall effect driven by a non-vanishing Berry curvature in the noncolinear antiferromagnet Mn_3Ge . *Sci. Adv.* **2**, e1501870 (2016).
- Kiyohara, N., Tomita, T. & Nakatsuji, S. Giant anomalous Hall effect in the chiral antiferromagnet Mn_3Ge . *Phys. Rev. Appl.* **5**, 064009 (2016).
- Ikhlas, M. et al. Large anomalous Nernst effect at room temperature in a chiral antiferromagnet. *Nat. Phys.* **13**, 1085–1090 (2017).
- Li, X. et al. Anomalous Nernst and Righi-Leduc effects in Mn_3Sn : Berry curvature and entropy flow. *Phys. Rev. Lett.* **119**, 056601 (2017).
- Xu, L. et al. Finite-temperature violation of the anomalous transverse Wiedemann-Franz law. *Sci. Adv.* **6**, eaaz3522 (2020).
- Sugii, K. et al. Anomalous thermal Hall effect in the topological antiferromagnetic state. <https://doi.org/10.48550/arXiv.1902.06601> (2019).
- Higo, T. et al. Large magneto-optical Kerr effect and imaging of magnetic octupole domains in an antiferromagnetic metal. *Nat. Photon.* **12**, 73–78 (2018).
- Balk, A. L. et al. Comparing the anomalous Hall effect and the magneto-optical Kerr effect through antiferromagnetic phase transitions in Mn_3Sn . *Appl. Phys. Lett.* **114**, 032401 (2019).
- Li, X. et al. Momentum-space and real-space Berry curvatures in Mn_3Sn . *SciPost Phys.* **5**, 063 (2018).
- Rout, P. K., Madduri, P. V. P., Manna, S. K. & Nayak, A. K. Field-induced topological Hall effect in the noncoplanar triangular antiferromagnetic geometry of Mn_3Sn . *Phys. Rev. B* **99**, 094430 (2019).
- Li, X. et al. Chiral domain walls of Mn_3Sn and their memory. *Nat. Commun.* **10**, 1–7 (2019).
- Xu, L., Li, X., Ding, L., Behnia, K. & Zhu, Z. Planar Hall effect caused by the memory of antiferromagnetic domain walls in Mn_3Ge . *Appl. Phys. Lett.* **117**, 222403 (2020).
- Liu, J. & Balents, L. Anomalous Hall Effect and Topological Defects in Antiferromagnetic Weyl Semimetals: $\text{Mn}_3\text{Sn}/\text{Ge}$. *Phys. Rev. Lett.* **119**, 087202 (2017).
- Kuroda, K. et al. Evidence for magnetic Weyl fermions in a correlated metal. *Nat. Mater.* **16**, 1090–1095 (2017).
- Šmejkal, L., Mokrousov, Y., Yan, B. & MacDonald, A. H. Topological antiferromagnetic spintronics. *Nat. Phys.* **14**, 242–251 (2018).
- Baltz, V. et al. Antiferromagnetic spintronics. *Rev. Mod. Phys.* **90**, 015005 (2018).
- Kimata, M. et al. Magnetic and magnetic inverse spin Hall effects in a non-collinear antiferromagnet. *Nature* **565**, 627–630 (2019).

36. Tsai, H. et al. Electrical manipulation of a topological anti-ferromagnetic state. *Nature* **580**, 608–613 (2020).
37. Li, X., Zhu, Z. & Behnia, K. A monomaterial Nernst thermopile with hermaphroditic legs. *Adv. Mater.* **33**, 2100751 (2021).
38. Ortiz, B. R. et al. CsV₃Sb₅: A \mathbb{Z}_2 topological Kagome metal with a Superconducting Ground State. *Phys. Rev. Lett.* **125**, 247002 (2020).
39. Yang, S.-Y. et al. Giant, unconventional anomalous Hall effect in the metallic frustrated magnet candidate, KV₃Sb₅. *Sci. Adv.* **6**, eabb6003 (2020).
40. Yin, J.-X. et al. Quantum-limit Chern topological magnetism in TbMn₆Sn₆. *Nature* **583**, 533–536 (2020).
41. Zhang, H. et al. Exchange-biased topological transverse thermoelectric effects in a Kagome ferrimagnet. *Nat. Commun.* **13**, 1091 (2022).
42. Jones, D. C. et al. Origin of spin reorientation and intrinsic anomalous Hall effect in the kagome ferrimagnet TbMn₆Sn₆. <https://doi.org/10.48550/arXiv.2203.17246> (2022).
43. Tomiyoshi, S. & Yamaguchi, Y. Magnetic structure and weak ferromagnetism of Mn₃Sn studied by polarized neutron diffraction. *J. Phys. Soc. Jpn.* **51**, 2478–2486 (1982).
44. Li, X. et al. The free energy of twisting spins in Mn₃Sn. <https://doi.org/10.48550/arXiv.2109.11122> (2021).
45. Chen, T. et al. Anomalous transport due to Weyl fermions in the chiral antiferromagnets Mn₃X, X= Sn, Ge. *Nat. Commun.* **12**, 1–14 (2021).
46. Balents, L. Anti-chiral order and spin reorientation transitions of triangle-based antiferromagnets. <https://doi.org/10.48550/arXiv.2204.01999> (2022).
47. Suzuki, M.-T., Koretsune, T., Ochi, M. & Arita, R. Cluster multipole theory for anomalous Hall effect in antiferromagnets. *Phys. Rev. B* **95**, 094406 (2017).
48. Behnia, K. & Aubin, H. Nernst effect in metals and superconductors: a review of concepts and experiments. *Rep. Prog. Phys.* **79**, 046502 (2016).
49. Ding, L. et al. Intrinsic anomalous Nernst effect amplified by disorder in a half-metallic semimetal. *Phys. Rev. X* **9**, 041061 (2019).
50. Xu, L. et al. Anomalous transverse response of Co₂MnGa and universality of the room-temperature $\alpha_{ij}^A/\sigma_{ij}^A$ ratio across topological magnets. *Phys. Rev. B* **101**, 180404 (2020).

Acknowledgements

This work was supported by The National Key Research and Development Program of China (Grant No. 2022YFA1403503), the National Science Foundation of China (Grant No. 12004123, 51861135104 and 11574097) and the Fundamental Research Funds for the Central Universities (Grant no. 2019kfyXMBZ071). B.Y. acknowledges funding from the European Research Council (ERC) under the European Union's Horizon 2020 research and innovation programme (ERC Consolidator Grant "NonlinearTopo", No. 815869). K.B. was supported by the Agence

Nationale de la Recherche (ANR-18-CE92-0020-01; ANR-19-CE30-0014-04). B.Y. and K.B. acknowledge a research grant from the Potter's Wheel Foundation/Weizmann-CNRS collaboration program. X.L. acknowledges the China National Postdoctoral Program for Innovative Talents (Grant No. BX20200143) and the China Postdoctoral Science Foundation (Grant No. 2020M682386).

Author contributions

X.L., Z.Z., K.B. and B.Y. conceived of and designed the study. X.L. performed the transport measurements. J.K. and B.Y. performed the theoretical calculations. X.L., J.K., Z.Z., K.B. and B.Y. analyzed the data. X.L., Z.Z., K.B. and B.Y. wrote the manuscript with assistance from all the authors.

Competing interests

The authors declare no competing interests.

Additional information

Supplementary information The online version contains supplementary material available at <https://doi.org/10.1038/s41467-023-37076-w>.

Correspondence and requests for materials should be addressed to Xiaokang Li, Zengwei Zhu or Binghai Yan.

Peer review information *Nature Communications* thanks the anonymous reviewer(s) for their contribution to the peer review of this work. Peer reviewer reports are available.

Reprints and permissions information is available at <http://www.nature.com/reprints>

Publisher's note Springer Nature remains neutral with regard to jurisdictional claims in published maps and institutional affiliations.

Open Access This article is licensed under a Creative Commons Attribution 4.0 International License, which permits use, sharing, adaptation, distribution and reproduction in any medium or format, as long as you give appropriate credit to the original author(s) and the source, provide a link to the Creative Commons license, and indicate if changes were made. The images or other third party material in this article are included in the article's Creative Commons license, unless indicated otherwise in a credit line to the material. If material is not included in the article's Creative Commons license and your intended use is not permitted by statutory regulation or exceeds the permitted use, you will need to obtain permission directly from the copyright holder. To view a copy of this license, visit <http://creativecommons.org/licenses/by/4.0/>.

© The Author(s) 2023